Experimental Investigation and Numerical Simulation on the Crack Initiation and Propagation of Rock With Pre-Existing Cracks

XUN XI[ID][1,2], XU WU[1,3], QIFENG GUO[1], AND MEIFENG CAI[1]

[1]School of Civil and Resource Engineering, University of Science and Technology Beijing, Beijing 100083, China
[2]Department of Civil and Environmental Engineering, University of Strathclyde, Glasgow G1 1XJ, U.K.
[3]Beijing Municipal Engineering Research Institute, Beijing 100037, China

Corresponding author: Qifeng Guo (guoqifeng@ustb.edu.cn)

ABSTRACT Rock mass behavior is determined not only by the properties of the rock matrix but also mostly by the pre-existing cracks in the rock mass. Before the overall failure of rock, the crack initiation and propagation around the tip of pre-existing cracks (i.e., pre-crack) will occur and contribute to rock failure. In this paper, the deep granite from a gold mine is taken and made to specimens with the pre-crack of 0.3 mm thickness. Uniaxial compression tests are carried out on the pre-cracked specimens. The acoustic emission (AE) sensors and digital image correlation (DIC) system are employed to record the failure characteristics of the specimens. The extended finite element method (XFEM) with the non-local stress field calculation is used to simulate the crack initiation and propagation of pre-cracks. The crack patterns, opening and shearing displacements of the cracked surface, and the crack length development are obtained from numerical simulations. Finally, the effects of friction of crack surface on the crack pattern and crack propagation are investigated and discussed. It has been found that, for pre-cracked specimens, crack initiation and propagation will occur when the stress is much smaller than the rock compressive strength. And in the range of pre-crack angle 30-60°, the larger the pre-crack angle is, the larger the compressive strength is. The crack patterns from numerical simulations have a good agreement with those from experimented DIC results. Moreover, the order of crack propagation speed is consistent with the order of the compressive strength. The crack pattern and crack propagation are affected by the friction coefficient of the cracked surface.

INDEX TERMS Rock, XFEM, crack propagation, acoustic emission, failure analysis.

I. INTRODUCTION

Natural joints or fractures widely existed in rock significantly affect rock mechanical response under various loading condition, which can even cause serious engineering disasters (e.g., the roof falling, rock burst and landslides). Natural fractures usually occur in sets that are more or less parallel and regularly spaced and the oriented fractures decrease the strength and stiffness of the rock [1]–[5]. Therefore, it is attractive for physically understanding the mechanical behavior of rock with various pre-existing cracks (i.e., pre-cracks) [6]–[8].

The associate editor coordinating the review of this manuscript and approving it for publication was Paolo Bettini[ID].

Furthermore, detailed investigations based on experiments and numerical modeling of the pre-cracked rock fracture can contribute to further understanding of rock failure processes.

In the past decades, extensive experiments have been performed on the strength reduction and failure characteristics of rock by compressive tests of the pre-cracked specimens [1], [3], [8]–[10]. Yang *et al.* [11]–[13] carried out a series of uniaxial and triaxial compression tests of pre-cracked sandstone specimens. They found that the cracks initiated in the form of tensile cracks, and the ultimate failure modes were mixed tensile and shear failure. Lee and Jeon [8] carried out uniaxial compression tests on granite specimens with pre-cracks of 1 mm thickness and found that the failure of specimens were

caused by tensile cracks and followed shear cracks. Zhuang et al. [14] made rock-like specimens (i.e., cement materials) and the pre-crack was created by inserting a 1 mm steel sheet into the mold. The crack propagation behavior of the rock-like specimens with the filled and unfilled crack was investigated. Li et al. [9] made sandstone specimens with a 1 mm thickness pre-crack and employed an acoustic emission (AE) system to investigate the failure characteristics during uniaxial compression tests. Although many experiments have been conducted on pre-cracked rock failure, most of them concerned more about the crack patterns and failure characteristics. The effects of crack initiation and propagation on rock failure have not been fully discussed.

Numerical approaches including finite element method (FEM) [6], discrete element method (DEM), boundary element method (BEM) [3], extended finite element method (XFEM) [7], [14], peridynamics (PD) [13] have been used to model the mechanical behaviors of pre-cracked rock. Li et al. [6] employed FEM (RFPA2D) to simulate the failure of pre-cracked coal specimen and found that existence of a single flaw reduced both the uniaxial compressive strength and elastic modulus of the coal specimens. The particle-based discrete element method is one of the most popular numerical methods to model the crack initiation, growth and coalescence processes of rock with pre-cracks during compression loading [2], [4], [8], [10], [15]. However, the contact parameters between particles are hard to determine and the results from particle models are more about strength and failure characteristics of the pre-cracked rock. XFEM is a robust numerical technique for crack initiation and propagation problem, which achieves discontinuities (cracks) within finite elements and can model the arbitrary crack propagation without remeshing [16]–[18]. Xie et al. [7], [19] employed XFEM to simulate crack propagation of closed flaws in rock and found that the friction of crack surface can affect crack initiation and propagation of the pre-cracked rock. Zhuang et al. [14] modeling the crack initiation and propagation of the pre-crack in rock-like specimens by XFEM and found that the crack patterns from numerical simulations had a good agreement with those from experiments. However, most numerical models were based on the local stress field and discussed more on the crack patterns while the crack propagation processes, especially for the crack length growth and the effect of surface friction on cracking, have never been fully investigated. Therefore, there is a well justification for a comprehensive investigation on the crack initiation and propagation of rock specimens with the pre-crack based on experiments and numerical simulations.

In this paper, granite samples are first made to the cubic specimens (50 mm×50 mm×100 mm) with through pre-cracks (50 mm×20 mm×0.3 mm) by the water jet cutter and diamond wire cutter. The uniaxial compression tests are carried out on the pre-cracked specimens. AE monitoring system and digital image correlation technique are employed to record the AE events and surface strain evolution during the compressive loading. The strength, AE characteristics and

crack pattern of the specimens are obtained and discussed. XFEM models with the same dimensions of the experimental specimens are developed and the crack propagation based on the non-local stress field around the crack-tip is simulated. The crack patterns, opening and shearing displacements of the cracked surface, and crack length development are investigated. Moreover, the effects of crack surface friction on the crack pattern and crack length development for the pre-cracked specimens are discussed.

II. EXPERIMENTAL PROGRAMME

Granite samples are taken from Sanshandao Gold mine, the mining depth of which has exceeded 1000 m. As shown in Figure 1, the granite consists of fine grains of plagioclase, potash feldspar, quartz and biotite. Although the joints and fissures are rich in the rock mass of Sanshandao Gold mine, the samples are well selected with no initial cracks. The average porosity of samples is about 1.29%.
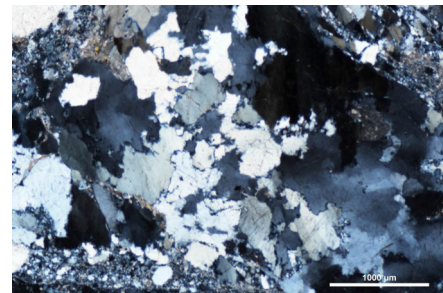

FIGURE 1. The micro structure of the granite under the microscope.

A. SPECIMEN PREPARATION

The granite specimens are cut to cubes with dimensions of 100 mm in height, 50 mm in length and 50 mm in width. The width or thickness of the natural crack in rock mass is generally very small [20]. Therefore, it is important to make a crack with a small width without disturbing the rock matrix. We employ the water jet cutter and diamond wire cutter to make the cracks as shown in Figure 2. First, a hole with diameter 2 mm is drilled by the water jet cutter in the center of the sample. Then, an inclined crack with dimensions of 20 mm in length and 0.3 mm in width is created by the diamond wire cutter. As shown in Figure 3, the rock samples with three crack inclination angles 30°, 45° and 60 ° are designed for mechanical tests.

B. TESTING PROCEDURES AND APPARATUS

Uniaxial compression tests are carried out on the GAW-2000 rigid testing machine. The loading is controlled by the apparatus displacement with a speed of 0.03 mm/min. During the loading process, acoustic emission (AE) monitoring and digital image correlation (DIC) techniques are employed to obtain the fracture characteristics of the specimens. The main technical parameters of compressive testing machine, AE and DIC apparatus are given in Table 1.
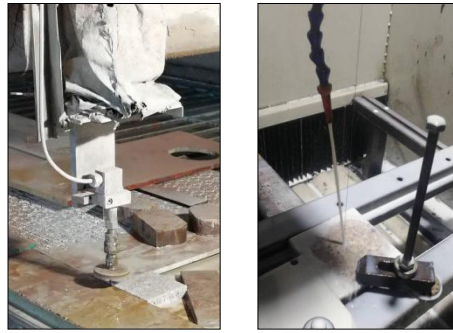
(a) The water jet cutter   (b) The diamond wire cutter

FIGURE 2. The specimen preparation processes: (a) drilling the hole by the water jet cutter; (b) making the pre-crack by the diamond wire cutter.

TABLE 1. The main technical parameters of the apparatus.

| Apparatus	Specification	Parameter	Value
Compression machine	GAW-2000	Maximum force	2000kN
		Accuracy	1%
		Loading rate	0.03mm/min
AE system	PCI-2	Frequency range	1kHz-3MHz
		Transmission speed	10M/second
		Threshold value	45-100dB
DIC system	VIC-3D	Measurement Resolution	5με
		Acquisition interval	0.2s
		Measurement Range	0.005%~2%
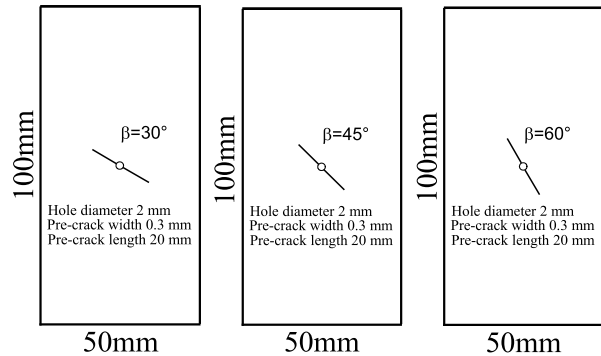
(a) Pre-crack angle 30°   (b) Pre-crack angle 45°   (c) Pre-crack angle 60°

FIGURE 3. Granite specimens with the inclined pre-cracks (a) pre-crack angle 30°; (b) pre-crack angle 45°; (c) pre-crack angle 60°.

As an optical, non-contact measurement technique, DIC is usually employed to obtain the displacement field on a specimen surface [21]. The speckled pattern was made on the specimen surface using ordinary black spray paint. Figure 4 shows the speckled specimen and DIC system. The pixel intensity correlation coefficient is calculated as follows [22]:

$$r(m,n) = \frac{\sum_i \sum_j F(i,j)T(i-m,j-n)}{\sqrt{\sum_i \sum_j [F(i,j)]^2}\sqrt{\sum_i \sum_j [T(i-m,j-n)]^2}}$$

(1)

where $r(m,n)$ is the pixel correlation parameter at location (m, n); F and T are the pixel greyscale values in the reference and deformed images, respectively.
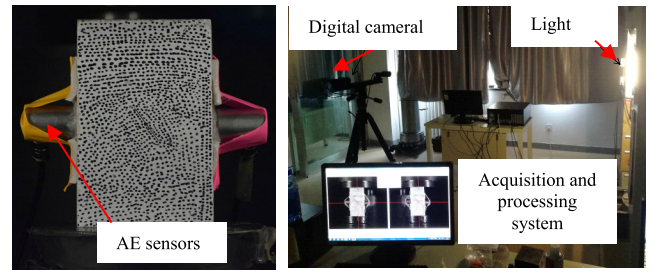
(a) The specimen   (b) The DIC system

FIGURE 4. Experimental setup: (a) The specimen for testing; (b) Digital image correlation system.

III. NUMERICAL METHOD

To overcome the problem associated with matching the geometry of the discontinuity as the crack propagation, the extended finite element method was first introduced by Belytschko and Black [23]. The presence of discontinuities is ensured by the special enriched functions in conjunction with additional degrees of freedom while the continuous displacements are derived from the traditional FEM with the retained sparsity and symmetry.

A. BASIC CONCEPTS OF XFEM

As shown in Figure 5, in XFEM, the Heaviside enrichment function and the crack tip enrichment functions are introduced to represent discontinuities and crack tip fields, respectively. Further, the total displacement can be expressed as follows [7], [24]:

$$u = \sum_{I=1}^{N} N_I(x)[u_I^{con} + H(x)a_I + \sum_{\alpha=1}^{4} F_\alpha(x)b_I^\alpha]$$

(2)

where u is the displacement in the computational domain; N is the number of the Gauss integral points in the domain. $N_I(x)$ is the continuous nodal shape functions; u_I^{con} is the continuous nodal displacement for the traditional finite element solution; $H(x)$ is the Heaviside function for achieving the displacement jump across the crack surface. a_I is the nodal enriched degree of freedom; $F_\alpha(x)$ is the asymptotic crack tip function. b_I^α is the nodal enriched degree of freedom.
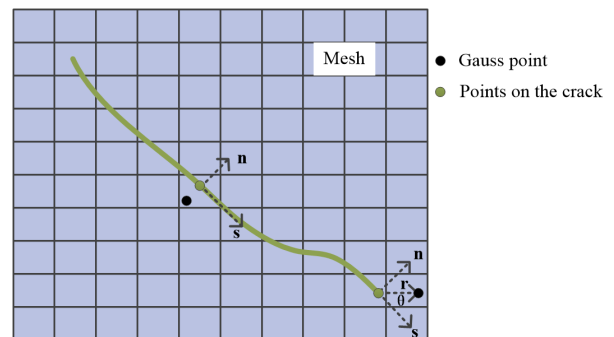
FIGURE 5. Illustration of normal and tangential coordinates for the crack.

The Heaviside function is expressed as follows:

$$H = \begin{cases} 1, & \text{if } (\mathbf{x} - \mathbf{x}^*) \cdot \mathbf{n} > 0 \\ -1, & \text{otherwise} \end{cases} \tag{3}$$

where $\mathbf{x}$ is a Gauss point; $\mathbf{x}^*$ is the closest point to $\mathbf{x}$ on the crack face. $\mathbf{n}$ is the unit outward normal to the crack at $\mathbf{x}^*$.

In a polar coordinate system (r, θ), the asymptotic crack tip function is expressed as follows:

$$F_\alpha = [\sqrt{r} \sin \frac{\theta}{2}, \sqrt{r} \cos \frac{\theta}{2}, \sqrt{r} \sin \theta \sin \frac{\theta}{2}, \sqrt{r} \sin \theta \cos \frac{\theta}{2}] \tag{4}$$

B. CONSTITUTIVE MODEL AND NON-LOCAL CRACK PROPOGATION

Rock exhibits the tensile strain softening behavior due to an inelastic zone being developed ahead of the crack tip, often referred to as fracture process zone (FPZ) [7], [25]. The cohesive crack model first proposed by Hillerborg et al. [26] has been employed to simulate discrete cracking in the fracture process zone of rock and concrete. As shown in Figure 6, post-peak softening behavior exhibits after reaching cohesive strength. In the XFEM modeling of rock fracture, cohesive crack model is used and the relationship between stress-displacement is expressed as follows:

$$\sigma = (1 - D)K\delta \tag{5}$$

where σ and δ are the cohesive stress and crack opening displacement, respectively; K is the elastic stiffness of the enriched element which can be specified as the Young's modulus of rock. D is the damage variable which is 0 before damage initiation and 1 after completely failure. The damage evolution between initiation of damage and final failure can follow a linear, exponential or tabular function [27].


(a) Illustration of the FPZ   (b) The stress-displacement curve
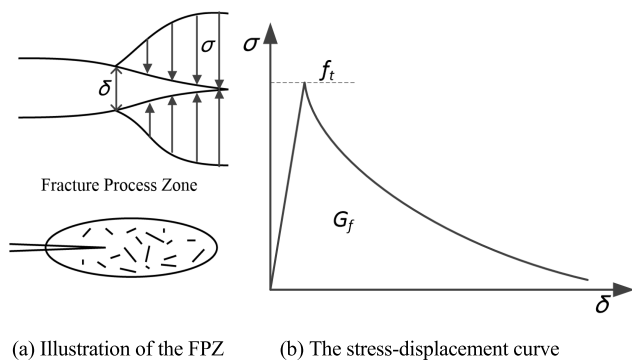
FIGURE 6. Constitutive relationship of rock cohesive crack:(a) Illustration of the FPZ; (b) The stress-displacement curve.

The damage initiation occurs when the maximum principal stress is larger than the tensile strength of rock. After reaching the cohesive strength, the tensile stress decreases, following certain softening rules. The softening behavior can be in a linear, bilinear or exponential curve. The area underneath the softening curve is known as the fracture energy G_f which can be measured by standard experiments [28]. Moreover,

the relationship between the fracture energy and fracture toughness can be established by Irwin's formula [29]:

$$K_{IC} = \sqrt{G_f \frac{E}{1 - \nu^2}} \tag{6}$$

There are two basic questions for modeling rock fracture: the crack initiation criteria and crack propagation direction. The crack initiation criteria have been developed above. Once the damage initiation criterion is satisfied, the newly introduced crack is always orthogonal to the maximum principal stress direction. However, the direction will be affected by the local element in the mesh. To reduce the mesh dependency and improve the accuracy of crack direction, a non-local calculation technique is used as illustrated in Figure 7. The elements in the radius of three times the typical element length are used to calculate the crack direction.
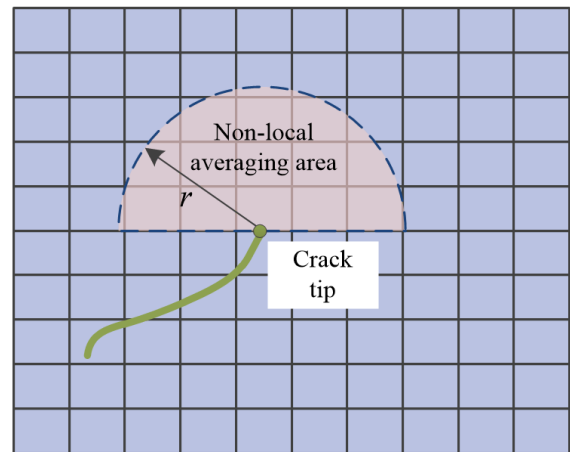
FIGURE 7. Non-local averaging of the stress for crack propagation.

C. NUMERICAL MODELS

Figure 8 shows the typical numerical model for rock specimen with the pre-crack angle 45°. The drilling holes with diameter 2 mm in the center of the specimens are created in the numerical models. The thickness of pre-crack is ignored and the friction of the pre-crack and newly created crack surface is set as 0.3 [7]. The basic parameters for the numerical models are listed in Table 2. The Young's modulus and poison's ratio are obtained by the uniaxial compressive tests of intact specimens. The tensile strength is obtained by Brazilian disk tests of intact specimens.

TABLE 2. Basic parameters for numerical simulations.

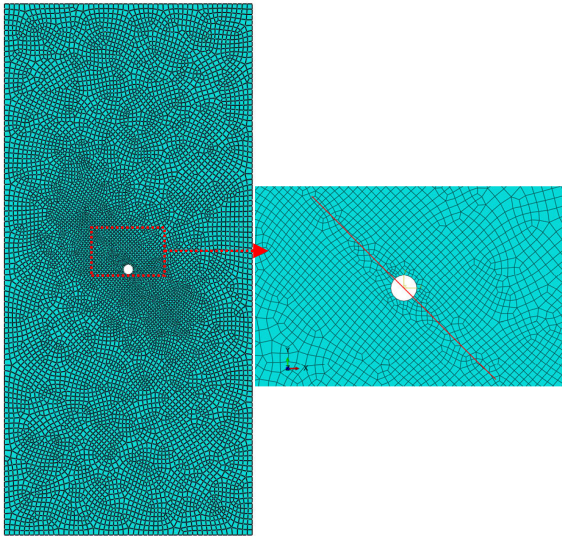| Description	Value
Young's modulus	28.46GPa
Poisson's ratio	0.25
Tensile strength	16 MPa
Fracture energy	200N/m [28]
Friction of cracked surface	0.3 [14]

FIGURE 8. The numerical model for the specimen with the pre-crack angle 45°.

IV. RESULTS AND DISCUSSION

Figure 9 illustrates the stress-strain curve and AE counts under the uniaxial compression tests for the specimens with the pre-crack angle 30°, 45° and 60°. It should be mentioned that, the strain is an overall strain which is equal to the loading displacement divided by the specimen length. It can be seen that, for all the specimens, with the strain increasing, the stress gradually increases until failure. For pre-cracked granite specimens, the AE events concentrate at several different values of strains while most AE events occurs just around the time to specimen failure. The concentrated AE events mean the micro/macro cracks initiation, accumulations and propagation. Therefore, for pre-cracked specimens, crack initiation and propagation will occur one or more times when the stress is much smaller than the rock compressive strength. The uniaxial compressive strength for the intact specimen is measured as 131.19MPa. While the uniaxial compressive strength of specimens with pre-crack angle 30°, 45° and 60° are 38.26MPa, 44.04MPa and 80.76MPa, respectively. The pre-crack significantly reduces the specimen compressive strength. And in the range of pre-crack angle 30-60°, the larger the pre-crack angle is, the larger the compressive strength is.

Figure 10 illustrates the typical DIC images for the crack propagations of the pre-cracked specimens. The contours are the maximum principal strains with values decreasing from largest (red) to smallest (blue). The crack patterns can be represented by the contours. It can be seen that the newly created cracks are wing cracks. The surface strains concentrate around the pre-crack dip and the cracks generally propagate towards the loading direction. For the specimen with pre-crack angle 30°, the slip of the pre-crack surface is limited while for others, the slip of the pre-crack surface is significant. The DIC technique is suitable to capture the crack patterns.
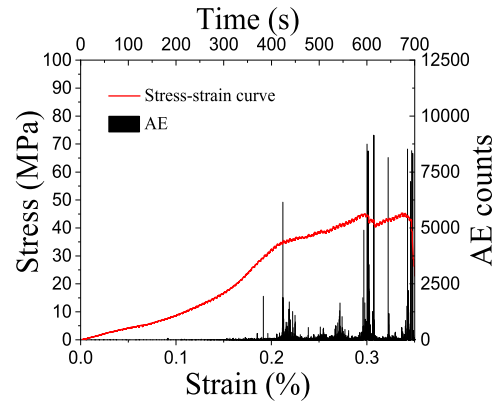
(a) Pre-crack angle 30°
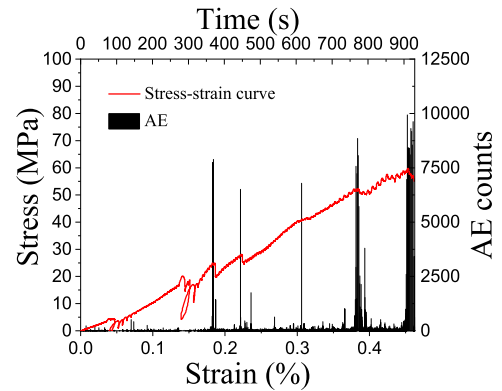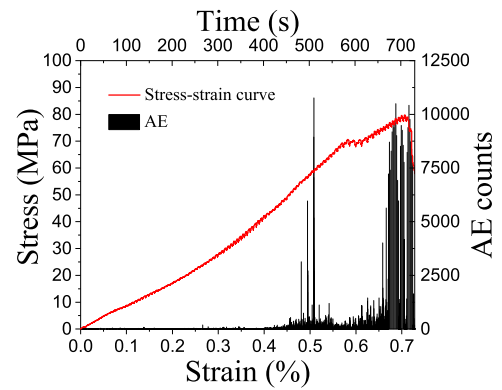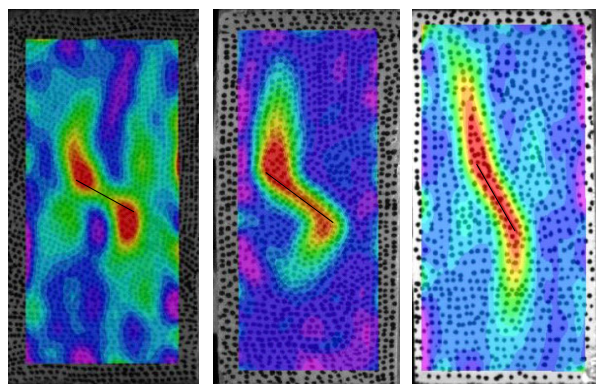

(b) Pre-crack angle 45°

(d) Pre-crack angle 60°

FIGURE 9. The stress-strain curves and AE histories during the compression tests for the specimens with (a) pre-crack angle 30°; (b) pre-crack angle 45°; (c) pre-crack angle 60°.

Figure 11 shows the maximum principal stress and crack propagation with the strain increasing for the specimen with pre-crack angle 45°. It can be seen that, the maximum principal stress concentrates around the crack tip. With the crack propagation, the stress concentration zone follows the crack tip. The crack pattern for the specimen with pre-crack angle 45° has a good agreement with the experimental results.

Figure 12 illustrates the opening and shearing displacements of the crack surface for the pre-cracked specimens. The opening and shearing displacement are obtained by writing

(a) Pre-crack angle 30° (b) Pre-crack angle 45° (c) Pre-crack angle 60°

FIGURE 10. DIC images of maximum principal strain for specimens with (a) pre-crack angle 30°; (b) pre-crack angle 45°; (c) pre-crack angle 60°.
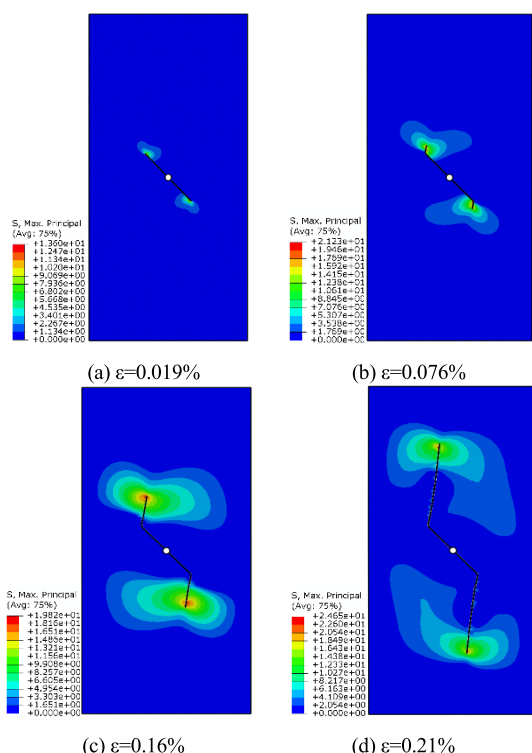

(a) ε=0.019%   (b) ε=0.076%

(c) ε=0.16%   (d) ε=0.21%

FIGURE 11. The maximum principal stress and crack propagation for the specimen with the pre-crack angle 45°.

(a) Pre-crack angle 30°

(b) Pre-crack angle 45°

(b) Pre-crack angle 60°

FIGURE 12. Opening and shearing displacement of the crack surface for the specimens with (a) pre-crack angle 30°; (b) pre-crack angle 45°; (c) pre-crack angle 60°.

ABAQUS keywords. It can be found that, the maximum opening displacements for the three models occur at the pre-crack tip while the maximum shearing displacements always occur at the surfaces of the pre-cracks. Because the slip between the crack surfaces always exists, it is necessary to consider the friction between the crack surfaces. It can be seen from the displacement contour that the opening displacements of the newly created cracks for all the specimens are much larger than the shearing displacements of those.

Figure 13 shows the crack patterns for the specimens. The crack paths are obtained by recording the cracked enriched elements with the damage value larger than 0.1, which is
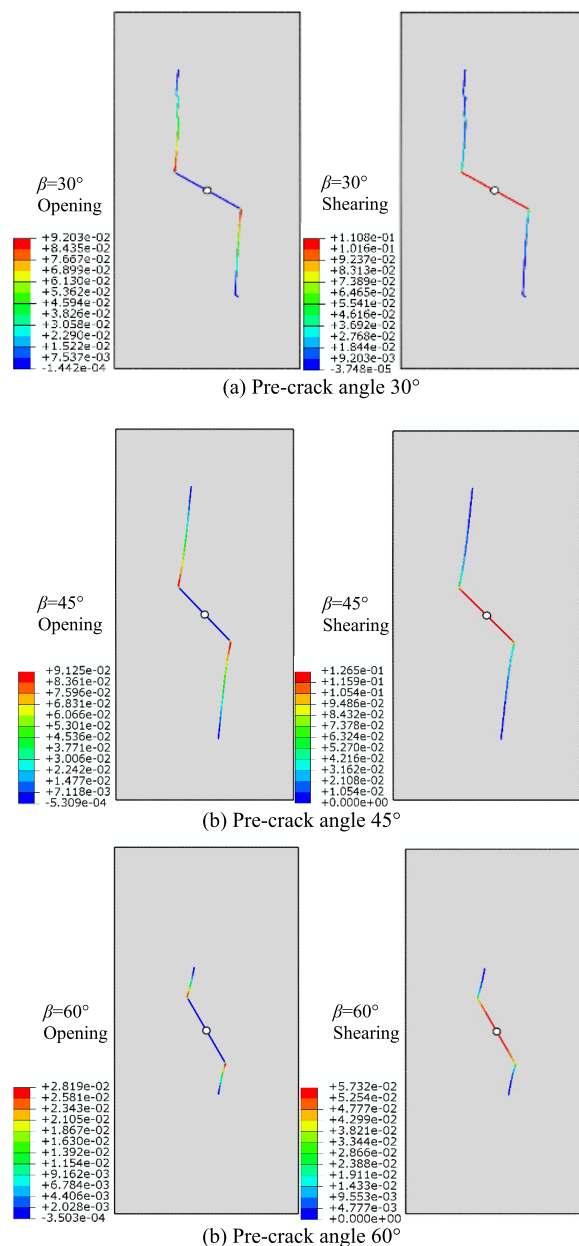
achieved by an in-house Python scripts. It can be seen that, the wing cracks initiate at the pre-crack tips and propagate towards the loading direction. With the increasing of pre-crack angle, the newly created crack defects clockwise. The crack patterns obtained from the numerical models have a good agreement with those from experiments (See Figure 10). The crack initiation angles vary with the pre-crack angles.

Figure 14 illustrates the developments of newly created crack length as a function of the strain for the specimens with pre-cracks. The crack length is calculated by the accumulated length of the cracked enriched elements, which is achieved by an in-house Python script. It can be found that, the wing
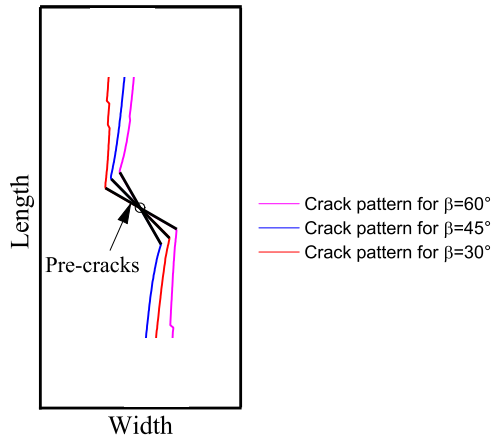
FIGURE 13. The crack patterns for the specimens with the pre-crack angles 30°, 45°, 60°.
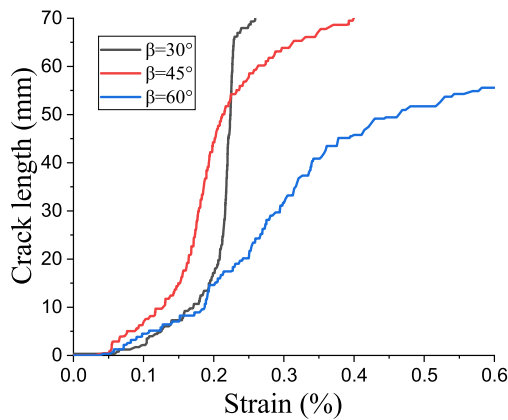

FIGURE 14. Newly created crack length development for the pre-cracked specimens.

FIGURE 15. The crack patterns of the specimen with the pre-crack angle 45° for different friction coefficients.

FIGURE 16. Newly created crack length development of the specimen with the pre-crack angle 45° for different friction coefficients.

cracks initiate when the strain is about 0.05% and then gradually increase. It is interesting to find that, the growth speeds of the wing cracks are different and the order of growth speed is: the specimen with pre-crack angle 30°, 45° and 60°. The order of growth speed of crack length is consistent with the order of the compressive strength. Moreover, the crack length for the specimen with pre-crack angle 60° is significantly smaller than that for others. The compressive strength of the specimen with pre-crack angle is also much larger than that for others. Therefore, the wing crack length growth can be closely related to the failure of the rock with pre-cracks.

The rough surface of newly generated cracks will affect the further crack process. Figure 15 shows the crack patterns for the specimen with the pre-crack angle 45° under different values of friction coefficient. The friction coefficient depends on rock type and surface roughness. In this paper, the values of friction coefficient are set as 0.1, 0.3 and 0.5 for comparisons [7]. It has been found that, the larger the friction coefficient is, the larger the angle between the pre-crack and new crack is.

Figure 16 illustrates the crack propagation of the specimen with the pre-crack angle 45° under the friction coefficient 0.1, 0.3 and 0.5. Obviously, the smaller the friction coefficient of
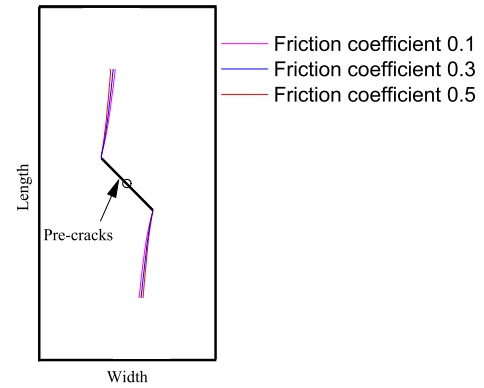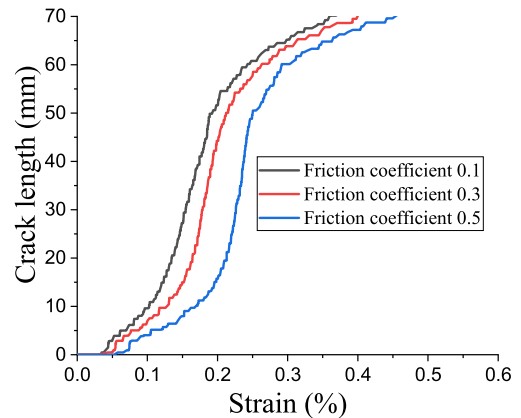
the crack surface is, the faster the crack propagation speed is. Therefore, the crack initiation and propagation of the pre-cracked rock are affected by the friction of the crack surface which may be related to the minerals and microstructures of the rock.

V. CONCLUSION

In this paper, granite samples from a deep gold mine were made to cubic specimens with pre-cracks by the advanced cutting machines. The uniaxial compression tests were carried out on the specimens with the pre-crack angle 30°, 45° and 60°. During the mechanical tests, AE events and surface strain were recorded by the AE monitoring system and the DIC technique. The crack initiation and propagation were modeled by XFEM with the non-local stress field calculation. The crack patterns, opening and shearing displacements of the cracked surface, and the crack length development are obtained from numerical simulations. Finally, the effects of surface friction on the crack pattern and crack length development are investigated and discussed. Experimental results showed that, for pre-cracked specimens, crack initiation and propagation will occur one or more times when the stress is much smaller than the rock compressive strength. And in the range of pre-crack angle 30-60°, the larger the pre-crack angle is, the larger the compressive strength is. The crack

patterns from numerical simulations have a good agreement with those from experimented DIC results. The opening displacements of the newly created cracks for all the specimens are much larger than the shearing displacements of those. Moreover, the order of growth speed of crack length is consistent with the order of the compressive strength. The larger the friction of the crack surface, the slower the crack propagation speed is.

REFERENCES

[1] S.-Q. Yang, P.-F. Yin, Y.-C. Zhang, M. Chen, X.-P. Zhou, H.-W. Jing, and Q.-Y. Zhang, "Failure behavior and crack evolution mechanism of a non-persistent jointed rock mass containing a circular hole," *Int. J. Rock Mech. Mining Sci.*, vol. 114, pp. 101–121, Feb. 2019.

[2] R.-H. Cao, P. Cao, H. Lin, X. Fan, C. Zhang, and T. Liu, "Crack initiation, propagation, and failure characteristics of jointed rock or rock-like specimens: A review," *Adv. Civil Eng.*, vol. 2019, pp. 1–31, Feb. 2019.

[3] A. Bobet, "The initiation of secondary cracks in compression," *Eng. Fract. Mech.*, vol. 66, no. 2, pp. 187–219, May 2000.

[4] J. Duriez, L. Scholtès, and F.-V. Donzé, "Micromechanics of wing crack propagation for different flaw properties," *Eng. Fract. Mech.*, vol. 153, pp. 378–398, Mar. 2016.

[5] Q. Guo, J. Pan, M. Cai, and Y. Zhang, "Investigating the effect of rock bridge on the stability of locked section slopes by the direct shear test and acoustic emission technique," *Sensors*, vol. 20, no. 3, p. 638, Jan. 2020.

[6] D. Li, E. Wang, X. Kong, M. Ali, and D. Wang, "Mechanical behaviors and acoustic emission fractal characteristics of coal specimens with a pre-existing flaw of various inclinations under uniaxial compression," *Int. J. Rock Mech. Mining Sci.*, vol. 116, pp. 38–51, Apr. 2019.

[7] Y. Xie, P. Cao, J. Liu, and L. Dong, "Influence of crack surface friction on crack initiation and propagation: A numerical investigation based on extended finite element method," *Comput. Geotechnics*, vol. 74, pp. 1–14, Apr. 2016.

[8] H. Lee and S. Jeon, "An experimental and numerical study of fracture coalescence in pre-cracked specimens under uniaxial compression," *Int. J. Solids Struct.*, vol. 48, no. 6, pp. 979–999, Mar. 2011.

[9] S. Li, D. Zhang, X. Bai, X. Zhang, Y. Chu, and K. Guo, "Experimental study on mechanical properties, acoustic emission energies and failure modes of pre-cracked rock materials under uniaxial compression," *Pure Appl. Geophys.*, vol. 176, no. 10, pp. 4519–4532, Oct. 2019.

[10] S.-Q. Yang, W.-L. Tian, Y.-H. Huang, Z.-G. Ma, L.-F. Fan, and Z.-J. Wu, "Experimental and discrete element modeling on cracking behavior of sandstone containing a single oval flaw under uniaxial compression," *Eng. Fract. Mech.*, vol. 194, pp. 154–174, May 2018.

[11] S. Q. Yang, Y. Z. Jiang, W. Y. Xu, and X. Q. Chen, "Experimental investigation on strength and failure behavior of pre-cracked marble under conventional triaxial compression," *Int. J. Solids Struct.*, vol. 45, no. 17, pp. 4796–4819, Aug. 2008.

[12] S.-Q. Yang and H.-W. Jing, "Strength failure and crack coalescence behavior of brittle sandstone samples containing a single fissure under uniaxial compression," *Int. J. Fract.*, vol. 168, no. 2, pp. 227–250, Apr. 2011.

[13] S.-Q. Yang, Z. Yang, P.-C. Zhang, and W.-L. Tian, "Experiment and peridynamic simulation on cracking behavior of red sandstone containing a single non-straight fissure under uniaxial compression," *Theor. Appl. Fract. Mech.*, vol. 108, Aug. 2020, Art. no. 102637.

[14] X. Zhuang, J. Chun, and H. Zhu, "A comparative study on unfilled and filled crack propagation for rock-like brittle material," *Theor. Appl. Fract. Mech.*, vol. 72, pp. 110–120, Aug. 2014.

[15] W. Zeng, S.-Q. Yang, and W.-L. Tian, "Experimental and numerical investigation of brittle sandstone specimens containing different shapes of holes under uniaxial compression," *Eng. Fract. Mech.*, vol. 200, pp. 430–450, Sep. 2018.

[16] N. Duan, W. Xu, S. Wang, and J. Zhu, "Quasi-3-D cylindrical coordinate XFEM model of HTS cable," *IEEE Trans. Magn.*, vol. 55, no. 6, pp. 1–4, Jun. 2019.

[17] F. Cruz, D. Roehl, and E. D. A. Vargas, "An XFEM implementation in abaqus to model intersections between fractures in porous rocks," *Comput. Geotechnics*, vol. 112, pp. 135–146, Aug. 2019.

[18] J. A. R. Cordero, E. C. M. Sanchez, D. Roehl, and L. C. Pereira, "Hydro-mechanical modeling of hydraulic fracture propagation and its interactions with frictional natural fractures," *Comput. Geotechnics*, vol. 111, pp. 290–300, Jul. 2019.

[19] Y. Xie, P. Cao, J. Jin, and M. Wang, "Mixed mode fracture analysis of semi-circular bend (SCB) specimen: A numerical study based on extended finite element method," *Comput. Geotechnics*, vol. 82, pp. 157–172, Feb. 2017.

[20] J.-A. Wang, Y.-X. Wang, Q.-J. Cao, Y. Ju, and L.-T. Mao, "Behavior of microcontacts in rock joints under direct shear creep loading," *Int. J. Rock Mech. Mining Sci.*, vol. 78, pp. 217–229, Sep. 2015.

[21] W. Dong, Z. Wu, X. Zhou, N. Wang, and G. Kastiukas, "An experimental study on crack propagation at rock-concrete interface using digital image correlation technique," *Eng. Fract. Mech.*, vol. 171, pp. 50–63, Feb. 2017.

[22] D. Corr, M. Accardi, L. Graham-Brady, and S. Shah, "Digital image correlation analysis of interfacial debonding properties and fracture behavior in concrete," *Eng. Fract. Mech.*, vol. 74, nos. 1–2, pp. 109–121, Jan. 2007.

[23] T. Belytschko and T. Black, "Elastic crack growth in finite elements with minimal remeshing," *Int. J. Numer. Methods Eng.*, vol. 45, no. 5, pp. 601–620, Jun. 1999.

[24] *ABAQUS 6.13, User Documentation*, Dessault Syst., Vélizy-Villacoublay, France, 2013.

[25] X. Xi, S. Yang, and C.-Q. Li, "A non-uniform corrosion model and meso-scale fracture modelling of concrete," *Cement Concrete Res.*, vol. 108, pp. 87–102, Jun. 2018.

[26] A. Hillerborg, M. Modéer, and P.-E. Petersson, "Analysis of crack formation and crack growth in concrete by means of fracture mechanics and finite elements," *Cement Concrete Res.*, vol. 6, no. 6, pp. 773–781, Nov. 1976.

[27] X. Xi, S. Yang, C.-Q. Li, M. Cai, X. Hu, and Z. K. Shipton, "Meso-scale mixed-mode fracture modelling of reinforced concrete structures subjected to non-uniform corrosion," *Eng. Fract. Mech.*, vol. 199, pp. 114–130, Aug. 2018.

[28] G. Vasconcelos, P. B. Lourenço, and M. F. M. Costa, "Mode I fracture surface of granite: Measurements and correlations with mechanical properties," *J. Mater. Civil Eng.*, vol. 20, no. 3, pp. 245–254, Mar. 2008.

[29] B. Carrier and S. Granet, "Numerical modeling of hydraulic fracture problem in permeable medium using cohesive zone model," *Eng. Fract. Mech.*, vol. 79, pp. 312–328, Jan. 2012.

XUN XI was born in Zhoukou, Henan, China, in 1991. He received the B.Eng. degree in mining engineering from the University of Mining and Technology, Beijing, in 2013, and the Ph.D. degree in civil engineering from the University of Science and Technology Beijing, in 2019.

He was a joint Ph.D. Student with the University of Strathclyde, U.K., from 2016 to 2018. He is currently a Research Associate with the Department of Civil and Environmental Engineering, University of Strathclyde. His research interests include rock and concrete fracture mechanics and durability problem for reinforced concrete structures and rockbolts.

XU WU was born in Zhangjiakou, Hebei, China, in 1988. He received the Ph.D. degree in engineering mechanics from the University of Science and Technology Beijing, in 2020. He is currently an Assistant Researcher/Professor with the Beijing Municipal Engineering Research Institute, China. His research interests include rock mechanics and subsurface engineering.

QIFENG GUO was born in Jiaozuo, Henan, China. He received the B.Eng. and Ph.D. degrees in mining engineering from the University of Science and Technology Beijing, China, in 2007 and 2012, respectively.

He was a Visiting Researcher with the Department of Civil, Environmental, and Geo-Engineering, University of Minnesota, USA, from 2017 to 2018. He is currently a Lecturer with the Department of Civil and Resource Engineering, University of Science and Technology Beijing. His research interests include the *in situ* stress measurements and rock mechanics.

MEIFENG CAI was born in Nantong, Jiangsu, China. He received the B.Eng. degree in engineering mechanics from Shanghai Jiao Tong University and the Ph.D. degree in rock mechanics from the University of New South Wales, Australia.

He is currently a Professor in civil engineering and mining engineering with the University of Science and Technology Beijing, China. He has published more than 200 scientific publications about *in situ* stress measurement, mining hazard control, and deep mining. He was elected as a Fellow of the Chinese Academy of Engineering, in 2013, for his contributions on the field of rock mechanics and mining engineering. He is the President of the Commission on Education of International Society for Rock Mechanics and Rock Engineering and the Vice President of the Chinese Society of Rock Mechanics and Engineering. He is also the Vice Editor-in-Chief of the *Journal of Rock Mechanics and Geotechnical Engineering*.

• • •